

Title	Three-dimensionally ordered hierarchically porous tin dioxide inverse opals and immobilization of palladium nanoparticles for catalytic applications
Authors	Collins, Gillian;Blömker, Martin;Osiak, Michal J.;Holmes, Justin D.;Bredol, Michael;O'Dwyer, Colm
Publication date	2013-10-09
Original Citation	Collins, G., Blömker, M., Osiak, M., Holmes, J. D., Bredol, M. and O'Dwyer, C. (2013) 'Three-Dimensionally Ordered Hierarchically Porous Tin Dioxide Inverse Opals and Immobilization of Palladium Nanoparticles for Catalytic Applications', Chemistry of Materials, 25(21), pp. 4312-4320. doi: 10.1021/cm402458v
Type of publication	Article (peer-reviewed)
Link to publisher's version	https://pubs.acs.org/doi/10.1021/cm402458v - 10.1021/cm402458v
Rights	© 2013 American Chemical Society. This document is the Accepted Manuscript version of a Published Work that appeared in final form in Chemistry of Materials, copyright © American Chemical Society after peer review and technical editing by the publisher. To access the final edited and published work see https://pubs.acs.org/doi/10.1021/cm402458v
Download date	2025-01-09 20:42:31
Item downloaded from	https://hdl.handle.net/10468/6154



UCC

University College Cork, Ireland
 Coláiste na hOllscoile Corcaigh

Article

Three-Dimensionally Ordered Hierarchically Porous Tin Dioxide Inverse Opals and Immobilization of Palladium Nanoparticles for Catalytic Applications

Gillian Collins, Martin Bloemker, Michal Osiak, Justin D Holmes, Michael Bredol, and Colm O'Dwyer

Chem. Mater., **Just Accepted Manuscript** • DOI: 10.1021/cm402458v • Publication Date (Web): 09 Oct 2013

Downloaded from <http://pubs.acs.org> on October 10, 2013

Just Accepted

"Just Accepted" manuscripts have been peer-reviewed and accepted for publication. They are posted online prior to technical editing, formatting for publication and author proofing. The American Chemical Society provides "Just Accepted" as a free service to the research community to expedite the dissemination of scientific material as soon as possible after acceptance. "Just Accepted" manuscripts appear in full in PDF format accompanied by an HTML abstract. "Just Accepted" manuscripts have been fully peer reviewed, but should not be considered the official version of record. They are accessible to all readers and citable by the Digital Object Identifier (DOI®). "Just Accepted" is an optional service offered to authors. Therefore, the "Just Accepted" Web site may not include all articles that will be published in the journal. After a manuscript is technically edited and formatted, it will be removed from the "Just Accepted" Web site and published as an ASAP article. Note that technical editing may introduce minor changes to the manuscript text and/or graphics which could affect content, and all legal disclaimers and ethical guidelines that apply to the journal pertain. ACS cannot be held responsible for errors or consequences arising from the use of information contained in these "Just Accepted" manuscripts.



ACS Publications
 High quality. High impact.

Three-Dimensionally Ordered Hierarchically Porous Tin Dioxide Inverse Opals and Immobilization of Palladium Nanoparticles for Catalytic Applications

G. Collins^{a,b,c}, M. Blömker^{d,e}, M. Osiak^{a,b}, J. D. Holmes^{a,b,c}, M. Bredol^e, and C. O'Dwyer^{a,b,d,*}

^a *Department of Chemistry, University College Cork, Cork, Ireland*

^b *Micro & Nanoelectronics Centre, Tyndall National Institute, Lee Maltings, Cork, Ireland*

^c *Centre for Research on Adaptive Nanostructures and Nanodevices, Trinity College Dublin, Dublin 2, Ireland*

^d *Materials and Surface Science Institute, University of Limerick, Limerick, Ireland*

^e *Department of Chemical Engineering, Münster University of Applied Sciences, Stegerwaldstraße 39, 48565 Steinfurt, Germany*

*To whom correspondence should be addressed: Tel: +353 (0)214902732. E-mail: c.odwyer@ucc.ie

Abstract

A high surface area 3D ordered SnO₂ inverted opal with walls composed of interconnected nanocrystals, is reported using a facile approach with a tin acetate. The hierarchically porous structure exhibits porosity on multiple lengths scales (cm down to nm). The thickness of the IO wall structure comprising nanocrystals of the oxide can be tuned by multiple infilling of the precursor. Using highly monodisperse Pd nanoparticles, we show how the SnO₂ IO can

be functionalized with immobilized Pd NP assemblies. We show that the Pd NP size dispersion is controlled by utilizing weak ligand-metal interactions and strong metal-oxide interactions for the immobilization step. The resulting SnO₂-Pd IOs were investigated X-ray photoelectron spectroscopy indicating electronic interactions between the Pd and SnO₂ and alterations to NP surface chemistry. Pd NPs assembled with excellent dispersion on the ordered SnO₂ IOs show superior catalytic performance for liquid phase chemical synthesis via Suzuki coupling reactions, and allow easy removal of the catalyst substrate post reaction. Higher mass electrocatalytic activity is also demonstrated for formic acid oxidation, superior to commercial Pd/C catalysts, which is shown to be due to better access to the catalytically active sites on SnO₂-Pd IOs. The high surface area interconnected phase-pure SnO₂ IO, with programmable porosity forms a functional material for catalytic applications.

Introduction

Semiconductor oxides with a 3-dimensional ordered macroporous (3-DOM), or inverse opal (IO) morphologies have gained much attention in recent years due to their unique structural features such as high surface area and programmable, ordered porosity¹. Tin dioxide (SnO₂) is a wide band gap semiconductor ($E_g \sim 3.6$ eV) with applications such as high capacity lithium battery anodes²⁻⁴, oxidation catalysts⁵, sensors^{6, 7} and optoelectronic devices^{8, 9}. Porous SnO₂ structures demonstrate superior sensing ability due to improved diffusion and higher surface area^{10, 11} and the periodic macroporous structure of SnO₂ IOs have shown to be a near ideal morphology for CO sensing applications¹². The use of hierarchical macroporous materials such as IOs are attractive materials for heterogeneous catalysts.¹³ Hierarchical porosity of 3-dimensionally ordered systems are beneficial for heterogeneous catalytic applications as they provide small pores for nanoparticle immobilization and the presence of

larger pore networks reduces mass transport limitations.¹⁴ Incorporation of mesoporosity into catalytic supports can lead to improved metal dispersion, greater active site accessibility and reaction rate enhancements.^{15, 16}

In addition to optimal structural properties of the support, size reduction of the metal nanoparticles is critical to their (electro)catalytic activity but controlling nanoparticle size and dispersion on solid supports remains challenging¹⁷. Supported catalysts prepared by impregnation or precipitation methods typically exhibit broad diameter distributions resulting from the annealing/reduction treatments required during synthesis. Solid-state synthesis through pyrolysis of organometallic precursors facilitates a single-step synthesis but controlling monodispersity is limited¹⁸. It is well recognized that excellent diameter control can be obtained through solution synthesis of colloidal nanoparticles.¹⁹ Achieving high catalyst loadings of colloidal nanoparticles often require pre-immobilization treatment of the support material such as oxidative or thermal activation or surface functionalization to introduce a chemical linker group^{20, 21}. A more significant drawback with colloidal nanoparticles is the presence of a capping layer, which is usually undesirable for catalytic applications and often needs to be removed by annealing treatments. Annealing, however generally results in loss of diameter control due to particle agglomeration.^{22, 23} Similarly, oxidative removal such as ozone treatment can lead changes in the surface chemistry of the metal.²⁴ Lopez-Sanchez *et al.*²⁵ demonstrated that up to 25% of polyvinyl alcohol (PVA) capping ligands on Au and AuPd NPs can be removed by solvent extraction thereby conserving the NP size and morphology.

In this paper we report the synthesis of 3D ordered, multi length scale porous SnO₂ IOs using tin acetate precursors, and the ability to functionalize the hierarchically porous network with Pd nanoparticles (NPs) with functional catalytic and electro catalytic behaviour. The use of the acetate as precursor avoids the need of corrosive SnCl₂ and moisture sensitive

tin alkoxide precursors, typically used for IO synthesis.^{11, 26} Furthermore, preparation of SnO₂ IO by the acetate produces structures with a hierarchical porosity making them ideal as catalyst support materials for liquids and gases.²⁷ We also report a facile method for the deposition of Pd nanoparticles with controlled diameter and size distribution. Immobilization of Pd nanoparticles onto these surfaces is then demonstrated without the need for post-annealing treatments to remove the capping ligands, which can be largely removed by solvent extraction in acetic acid. We demonstrate the viability of these SnO₂-Pd nanocomposites for catalytic applications. Firstly, the SnO₂-Pd IOs are demonstrated as functional catalytic coatings for chemical synthesis with Suzuki coupling reactions, which are important carbon-carbon bond forming reactions used extensively in pharmaceutical synthesis. The activity of SnO₂ Pd IOs as anodes for electrocatalytic oxidation of formic acid is also investigated. The use of oxide support materials for fuel cells are promising replacements for carbon supports which are susceptible to corrosion²⁶. SnO₂ is reported to display remarkably enhanced CO tolerance leading to lowering poisoning effects and also exhibit promotional effects due to electronic interactions between SnO₂ and the active metal.^{28, 29} The use of SnO₂ IOs as supports for Pd-catalyzed formic acid oxidation (FAO) has not been reported thus far, and they have potential for improved catalytic performance through increased surface area and hierarchical porosity.

2. Experimental

Polystyrene (PS) spheres (0.5 μm) were purchased from Polysciences Europe, Eppelheim, Germany. All other chemicals were purchased from Sigma-Aldrich.

2.1 Preparation of SnO₂ IO using Sn(II) and Sn(IV) acetates. Opal templates were purified by centrifugation of 5 ml of PS-spheres. The supernatant water was removed and the sample

was re-dispersed. Deposition of the spheres onto stainless steel substrates was carried out by electrophoretic deposition (EPD).³⁰ A 2.5 wt% solution of spheres in EtOH was prepared and NH₄OH solution was added dropwise to obtain a pH of 10. Two stainless steel substrates, placed 5 mm apart were used as the anode and cathode. To immobilize the templates, 2.5 V was applied for 1 h, followed by 150 V for 10-20 s. This procedure gave rise to templates of ~200 μ m thick. Infiltration of the polymer templates with SnO₂ was carried out using saturated solutions of Sn(II) or Sn(IV) acetate in acetic acid prepared by dissolving the maximum amount of the precursor salt in ~2 ml of acetic acid at 100 °C. The solution was cooled to room temperature under stirring before drop casing onto the polymer sphere template. Infiltrated templates were dried at 40°C for at least 2 hours in a drying oven. In case of multiple infiltrations, the infiltration procedure was repeated as often as necessary once the samples were dried and cooled to RT. Subsequently, the templates were dried at 40 °C for at least two hours until complete evaporation of the acetic acid after every infiltration step. To remove the PS spheres, the substrates were calcined in air at a temperature of 600 °C for 5 h. To study the effect of annealing rate on the IO structure, two annealing rates of 0.5 °C min⁻¹ and 5 °C min⁻¹ were used.

2.2 Synthesis and immobilization of Pd NPs. Pd NPs were synthesized using modified literature procedures^{31, 32}. The synthesis was carried out under Ar using standard Schlenk techniques. In a typical synthesis, 75 mg of Pd(acac)₂ was dissolved in 15 ml of oleylamine (OA) and heated to 60 °C under magnetic stirring. 1 ml of triphenylphosphine (TOP) was injected into the solution. In a separate flask, 300 mg of borane *t*-butylamine was dissolved in ~3 ml OA under Ar. This amine complex solution was then injected into the Pd precursor solution and heated to 90 °C. The reaction was aged for 3 h. After the solution cooled to room temperature, ethanol was added to precipitate the NPs, which were collected by

centrifuge. The precipitate was redispersed in 10 ml of hexane and a further 30 ml of EtOH was added to precipitate the NPs. The NPs were sonicated and collected by centrifugation at 8000 rpm. This purification procedure was repeated three times and the purified NPs were redispersed in hexane. After purification the typical mass of NPs obtained was 55-60 mg. Preparation of other NPs used in this study were prepared by literature methods and are described in the Supporting Information³³.

SnO₂ IOs were dried under vacuum overnight and then immersed in the NP solution. The mixture was briefly sonicated and agitated overnight. The SnO₂ IOs were removed from the NP solution without rinsing and dried in a vacuum oven for ~4 h at 60 °C followed by drying in air at 120 °C overnight. To clean the nanocomposite of residual NPs the IOs were immersed in fresh hexane solution and agitated for 30 min, followed by immersion into EtOH. The substrates were further rinsed in fresh EtOH and finally hexane, before being dried under vacuum at 60 °C.

2.3 Materials Characterization. Scanning Electron Microscopy (SEM) characterization was performed using a Hitachi S-4800 SEM cold field emission apparatus or a SU-70 SEM hot field emission apparatus. Transmission Electron Microscopy (TEM) and energy dispersive x-ray (EDX) spectroscopy was carried out using a JEM2010-TEM equip with an Oxford X-Max 80 detector and Inca analysis software. Fourier-transform Infrared (FTIR) was performed on a Nicolet 6700 FTIR. X-ray Photoelectron Spectroscopy (XPS) was acquired using a KRATOS AXIS 165 monochromatized X-ray photoelectron spectrometer equipped with an Al K α (h ν = 1486.6 eV) X-ray source. Spectra were collected at a take-off angle of 90° and all spectra were reference to the C 1s peak at 284.6 eV. The Sn 3d core level spectra were fit to Gaussian (70%)-Lorentzian (30%) profiles. The Pd 3d core level spectrum of the

unsupported NPs was fit to Gaussian (90%)-Lorentzian(10%) profile for elemental Pd centred at 334.1 eV with FWHM = 0.9. After immobilization of the Pd NPs onto SnO₂ IOs, the Pd 3d core level required different fitting parameters in order to obtain a satisfactory fit. The elemental Pd peak was centred at 335.5 eV and fit to a broader peak (FWHM = 1.2). The oxide associated Pd²⁺ and Pd⁴⁺ peaks were fit with FWHM = 1.5. The oxide thickness was calculated by the substrate overlayer model using Eqn 1.³⁴

$$d = \lambda_{ox} \cos \theta \ln \left(\frac{N_{Pd} \lambda_{Pd} I_{ox}}{N_{ox} \lambda_{ox} I_{Pd}} + 1 \right) \quad (1)$$

where λ is the effective photoelectron attenuation length, I_{Pd} and I_{Ox} are the photoelectron intensities of the Pd and PdO_x species, respectively, N is the number of atoms per unit volume and θ is the detection angle. The density of Pd and PdO was taken to be 12.08 g cm⁻³ and 8.3 g cm⁻³ respectively. The density of PdO₂ was estimated by structural data taking the unit cell volume to be 62.32 Å³.³⁵ The attenuation length (λ_{AL}) of Pd 3d electrons moving through the metallic core and oxide overlayer was estimated using the CS2 semi-empirical method developed by Cumpson and Seah,³⁶ and described by Eqn 2:

$$\lambda_{AL} = 0.31 a^{3/2} \left\{ \frac{E}{z^{0.45} \left[\ln \left(\frac{E}{27} \right) + 3 \right]} + 4 \right\} \quad (2)$$

where E is the kinetic energy (eV), a is the lattice constant or monolayer thickness and z is the average atomic number.

2.4 Catalytic performance of SnO₂-Pd nanocomposites.

Suzuki Cross Coupling: In a typical reaction, 2 mmol of aryl halide, 2.2 mmol of phenylboronic acid and 2 equivalents of K₂CO₃ was added to 30 ml of EtOH:H₂O (2:1) solvent. A stainless steel substrate coated SnO₂ Pd IO (typical dimension 0.8 cm × 3 cm) was

1
2
3 immersed vertically into the solution and clamped at the top. The solution was stirred during
4
5 the reaction which was carried out in air. Reactions were monitored by TLC. After the
6
7 reaction, the EtOH was removed by rotary evaporation and the product was extracted with
8
9 DCM ($\times 3$). The organic layer was washed with water ($\times 3$) and dried over MgSO_4 . The turn
10
11 over number (TON) and turn over frequencies (TOF) of the catalytic thin films was
12
13 calculated based on the mass of SnO_2 IO. Where the $\text{TON} = \text{mol of aryl halide converted}/$
14
15 mol Pd and the $\text{TOF} = \text{mol converted arly halide}/ \text{mol Pd h}^{-1}$. The Pd concentration was
16
17 determined by EDX analysis.
18
19

20
21 *Electrocatalytic studies:* The electrochemical properties of the supported catalysts was
22
23 carried out in a three-electrode cell at room temperature using a BioLogic VSP potentiostat.
24
25 A Pt wire mesh, Standard Calomel Electrode (SCE) and glassy carbon electrode were used as
26
27 the counter, reference and working electrodes, respectively. To prepare the working
28
29 electrode, the Pd SnO_2 IO catalysts were deposited on the electrode surface followed by a 10
30
31 μl droplet of 0.1 wt % Nafion solution. Linear sweep (LSV) and cyclic voltammograms
32
33 (CVs) of the catalysts were obtained in Ar saturated 0.1 M perchloric (HClO_4) and 2 M
34
35 formic acid (HCOOH) solution. The potential was scanned from -0.2 V to +1.0 V at a scan
36
37 rate of 10 mV s^{-1} . Unless otherwise stated, all potentials are referenced with respect to SCE.
38
39 The mass current was normalized to A/g Pd by dividing the measured electrode density over
40
41 the mass Pd in the catalysts.³⁷
42
43
44
45
46
47
48
49

50 Results and Discussion

51 *Synthesis of hierarchically porous SnO_2 IOs using tin acetate precursors*

52
53 Figure 1 shows SEM and TEM images of SnO_2 IOs synthesized with Sn(IV) acetate
54
55 precursors under different treatment conditions. Figure 1 (a) and (d) display SEM images of
56
57
58
59
60

the IOs obtained by double (successive) infiltration and annealing rate of $0.5\text{ }^{\circ}\text{C min}^{-1}$ and $5\text{ }^{\circ}\text{C min}^{-1}$, respectively. In this synthetic method, we find that faster annealing rates decrease the wall thickness from $\sim 60\text{ nm}$ at $0.5\text{ }^{\circ}\text{C min}^{-1}$ to $\sim 45\text{ nm}$ at $5\text{ }^{\circ}\text{C min}^{-1}$, as shown in the inset in figure 1 (a) and (d). The morphology of the walls annealed at $5\text{ }^{\circ}\text{C min}^{-1}$ also display rougher surfaces compared to those annealed at $0.5\text{ }^{\circ}\text{C min}^{-1}$, which is shown in the TEM image in figure 1 (b) and (e). Specifically, the seemingly rough walls of the 3-dimensionally ordered porous network comprises an assembly of nanoscale crystallites of SnO_2 with an average size of $\sim 5\text{ nm}$. All such crystals are single crystals and they are fused together at grain boundaries; this assembly of SnO_2 nanocrystals is itself porous. The detail of this fused structures can be seen in TEM image in figure 1 (c). The high resolution TEM in figure 1 (b) inset shows a particle with an interplaner d-spacing of 0.26 nm , which can be indexed to SnO_2 (101).³⁸

The number of precursor infiltrations influence the structures of the IOs with single infiltration often resulted in an incomplete IO network. The wall thickness of the IOs after a single infiltration were slightly thinner ($\sim 50\text{ nm}$) compared to IOs after a double infiltration due to a lower number of crystallites making up the thickness of the wall, but displayed similar nanocrystallite size (5 nm), shown in figure 1 (f)-(g). Three infiltrations of Sn acetates dissolved in acetic acid does completely infill in the PS template, however results in an irregular IO structure due to excess SnO_2 (Supporting Information, Figure S1).

SnO_2 IOs derived from the Sn(II) precursors have similar structure to those of Sn(IV) precursors in terms of the definite size of the nanocrystals and their arrangement to form porous walls of similar thickness (Supporting Information, Figure S1 (a)-(e)). SnO_2 IOs prepared from Sn(II) precursors also crystallize similarly to Sn(IV) acetates, with faster annealing rates resulting in thinner walls and smaller nanocrystalline size. The average nanocrystal size is smaller ($<5\text{ nm}$) and of higher density.

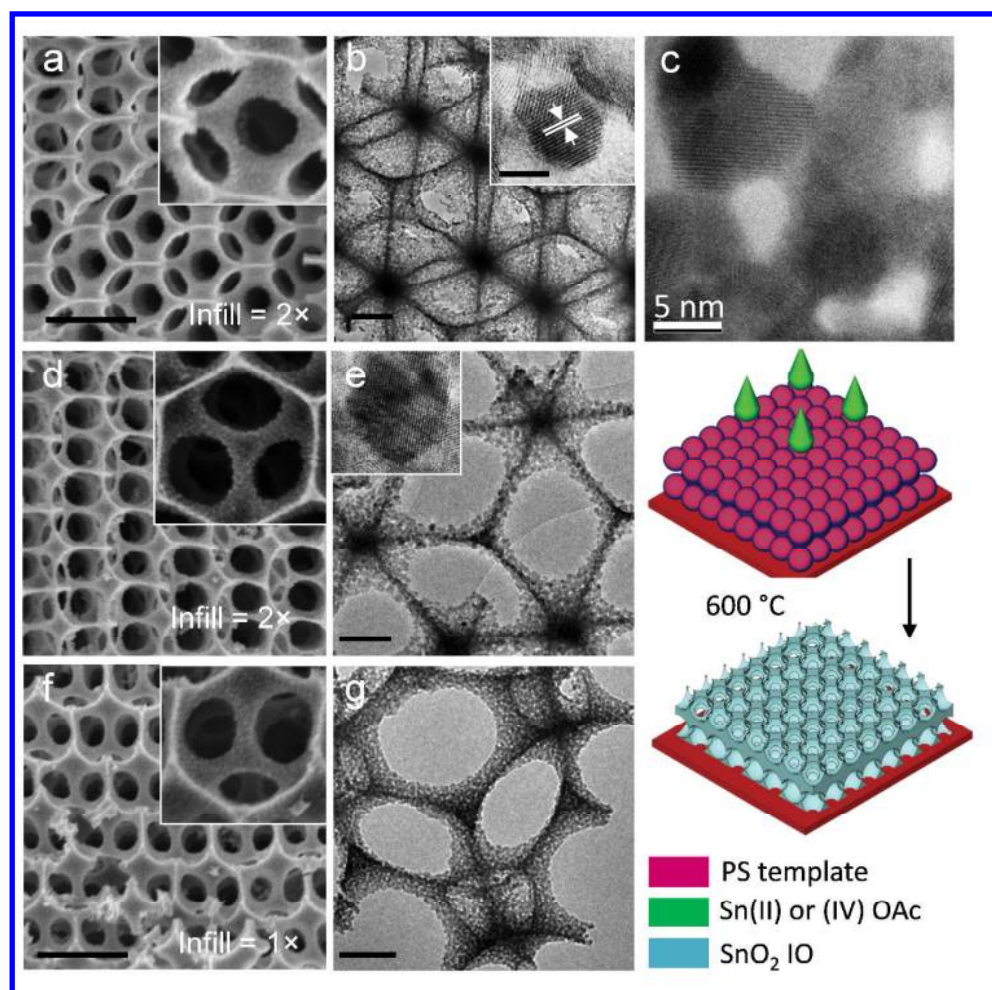
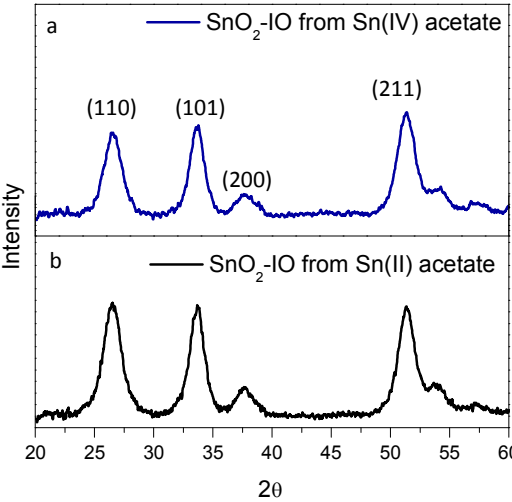


Figure 1. (a)-(b) SnO₂ IOs formed using double infiltration of a Sn(IV) acetate, calcined at 0.5 °C min. (c) HRTEM image of the fused arrangement of SnO₂ nanocrystals comprising the mesoporous walls of the IO. (d)-(e) SnO₂ IOs formed using double infiltration but crystallized at 5 °C min. A schematic to the right shows the arrangement of the original (111)-oriented fcc lattice of polymer sphere templates prepared by EPD and a definition of the hierarchical porosity for the porous 3D IOs. (f)-(g) SnO₂ IOs formed using single infiltration 0.5 °C min⁻¹ using Sn(IV) acetate. Scale bar in main figure (a), (d) and (f) are 500 nm and the scale bar in insets are 100 nm. Scale bar in figure (b), (e) and (g) are 100 nm.

The XRD characterization of crystal phase and purity of the IOs is shown in figure 2 (a)-(b). X-ray diffraction patterns showing peaks that are indexed to (110), (101), (200) and (211) reflections of tetragonal cassiterite phase SnO_2 (space group $P42/mnm$). Furthermore, the XRD pattern exhibits no additional peaks, indicating the absence of crystalline or heterophase impurities such as *e.g.* SnO . XPS analysis further confirms the presence of phase pure SnO_2 . The survey spectra of the IOs (Supporting Information Figure S2) show only the presence of Sn, oxygen and small amounts of remnant carbon. The Sn 3d core level spectra of the IOs shown in figure 2 (c)-(d) consist of a doublet located a binding energies of 486.1 eV and 494.5 eV, which can be assigned to the Sn $3d_{5/2}$ and Sn $3d_{3/2}$ of Sn^{4+} in SnO_2 , respectively.³⁹



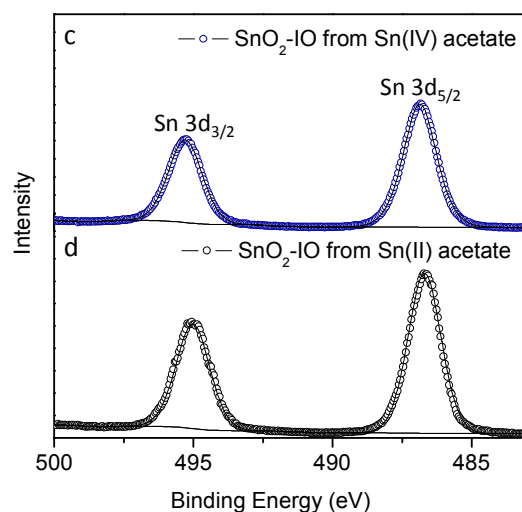


Figure 2. (a)-(b) XRD pattern of SnO₂-IO prepared from Sn(IV) acetate precursor and Sn(II) acetate precursor, respectively. The patterns can be indexed to JCPDS 00-041-1445. (c)-(d) Sn 3d core level XPS of SnO₂-IO from Sn(IV) acetate precursor and Sn(II) acetate precursor, respectively.

Palladium Immobilized SnO₂ IOs

Figure 3 illustrates the formation of the Pd NPs with an average diameter of 3.2 nm (standard dev. = 0.95) determined by size distribution analysis (Supporting Information, Figure S3). The XRD patterns (Supporting Information, Figure S4) for the Pd NPs shows the presence of 4 peaks at 40°, 46°, 68° and 80°, indexed to the (111), (200), (220) and (311) diffraction peaks of Pd, respectively. The FTIR spectra of neat OA and OA-capped Pd NPs are (Supporting Information Figure S5) are similar, except for shifts in the absorption peaks due to the interactions of OA with the Pd NPs.⁴⁰ The band at 3343 cm⁻¹ in the IR spectrum of OA assigned to the N–H stretching mode, is red-shifted to 3390 cm⁻¹ in OA-capped Pd NPs due to absorption of amine groups onto the Pd surface. The N–H bending band at 1570 cm⁻¹ in neat OA is also shifted to 1566 cm⁻¹ in the Pd NPs spectrum. No evidence for the

presence of phosphine ligands is observed in the IR spectrum of the OA-Pd NPs and XPS analysis shown in figure 3 further confirms the absence of phosphorous in the survey spectra (P $3p_{3/2}$ ~130 eV) indicating that phosphine ligands are not bound to the Pd surface. The presence of TOP during NP synthesis was found to be important for improving the monodispersity of the Pd NP size and shape consistency, as shown in the TEM of the NPs in figure 4(a). The use of dual co-ordinating ligands during NP synthesis can improve monodispersity due to their different binding affinity with the metal NP.⁴¹ Nanoparticles synthesized without addition of TOP led to a mixture of small diameter (< 5 nm) nanoparticles and larger aggregates and illustrated by TEM (Supporting Information, Figure S6).

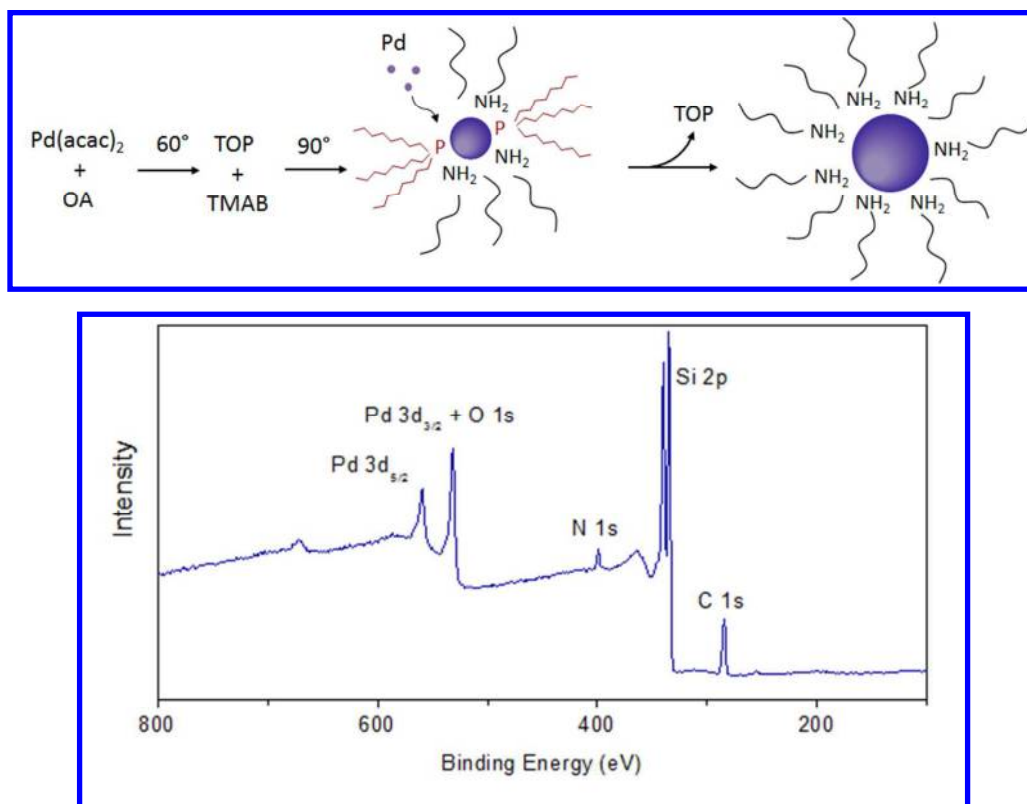


Figure 3. Schematic illustrating the steps in Pd NP formation in the presence of TOP and OA ligands. XPS survey spectra (100-800 eV) showing the absence of P capping ligands on the NPs. Note that the Si 2p peak arises from the Si wafer used to deposit the NPs for analysis.

Figure 4(b)-(c) shows highly dispersed Pd NPs immobilized on SnO₂ IO. High resolution TEM in figure 4(d) displays nanocrystals with an interplanar d-spacing of 0.33 nm and 0.26 nm, which can be indexed to SnO₂ (110) and SnO₂ (101), respectively³⁸. The lattice fringes with a d-spacing of 0.23 nm correspond to those of Pd(111)⁴². From figure 4(d), the Pd NPs are found to be dispersed primarily around the SnO₂ nanocrystals; no dominant facet relationships between the crystalline Pd and SnO₂ at the NP attachment sites is found and the arrangement is random in distribution. The density of Pd NPs appears highest at either side of the walls (figure 4(b)), but we find that the distribution is relatively consistent spatially, *i.e.* that the density of Pd particles that form a randomly distributed assembly either side of the IO walls is similar to the density of Pd NPs covering the SnO₂ nanocrystals comprising the walls. TEM analysis of several regions consistently shows that the Pd NPs are generally well disperse and do not aggregate or overlap after immobilization in a low dielectric constant non-polar solvent (Supporting Information, Figure S7-S8). Furthermore, the Pd NPs do not entirely cover the available surface area of the IO structure for the concentration of NPs used in the dispersion. EDX elemental mapping of the Pd SnO₂ IO is shown in figure 5 (a)-(c) confirms the presence of Pd NPs immobilized on the SnO₂ IOs, and quantitatively confirm the Pd NP dispersion and coverage of the hierarchically porous SnO₂ IO structure, which does not suffer extensive cracking even for a thickness of 100 μm. The Pd concentration determined by quantitative EDX analysis is 10.4 wt%. Cross-sectional SEM was used to assess the distribution profile of the Pd NPs through the SnO₂ IO in a thick, multi-layered IO. Figure 5 (d) shows EDX line-scans for Pd and Sn through a 200 μm thick IO matrix. The presence of Pd NPs is clearly identified through the IO network, and follows the distribution of Sn from the SnO₂, *i.e.* while there is less Pd than SnO₂ present in the IO, the distribution within the interaction volume probed by the electron beam is

consistent with the variation in the density of the matrix, indicating relatively uniform solution based dispersion (discussed below) through a very thin mesoporous matrix.

BET analysis of the SnO₂ IOs show a specific surface area of 35 m² g⁻¹, and a pore volume of 0.12 cm³ g⁻¹, consistent with reports of TiO₂ IOs.⁴³ A pore diameter of 13.5 nm indicates mesoporosity in the network.⁴⁴ After Pd NP deposition, the surface area increases to 48 m² g⁻¹ and a small decrease in the pore diameter (12 nm) was observed due to presence of the Pd NPs within the IO network.

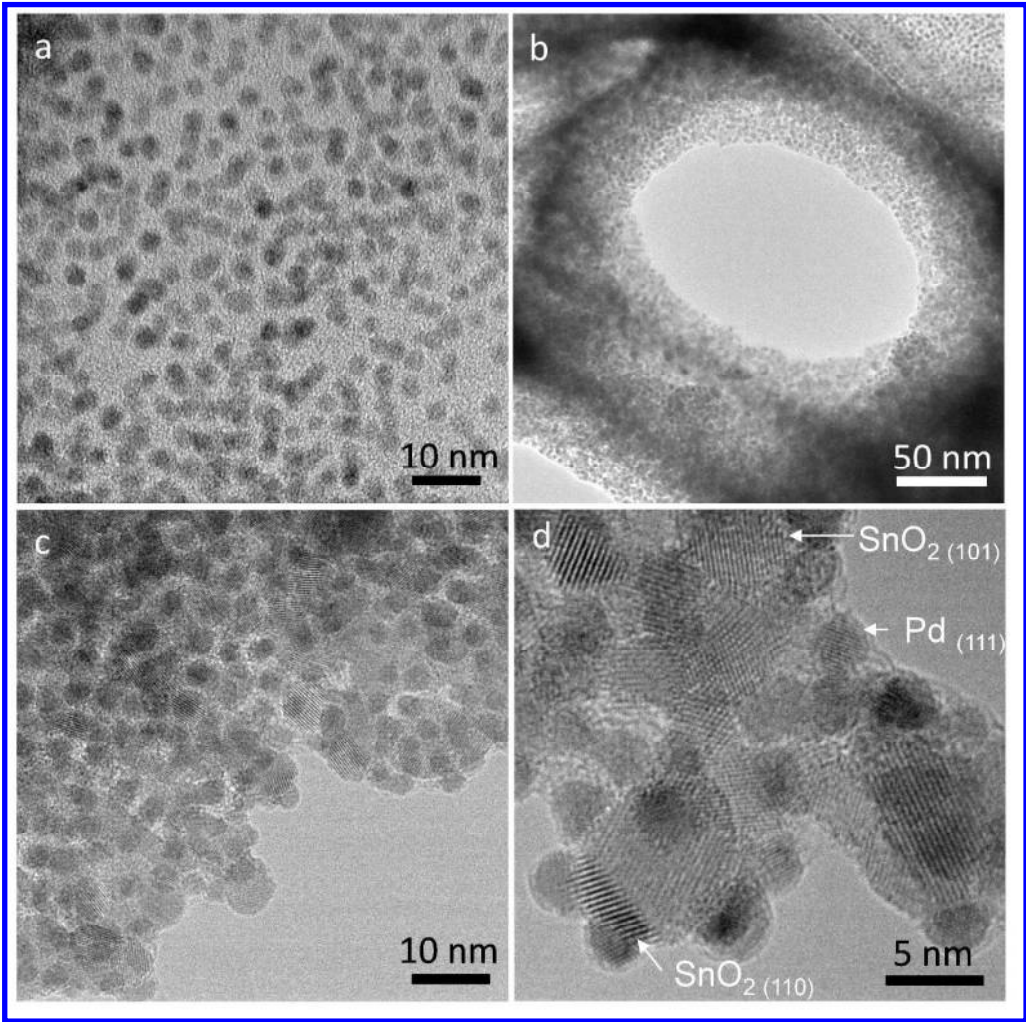


Figure 4. TEM images of (a) as-synthesized OA-capped Pd nanoparticles. (b)-(d) SnO₂ IOs after Pd nanoparticle immobilization.

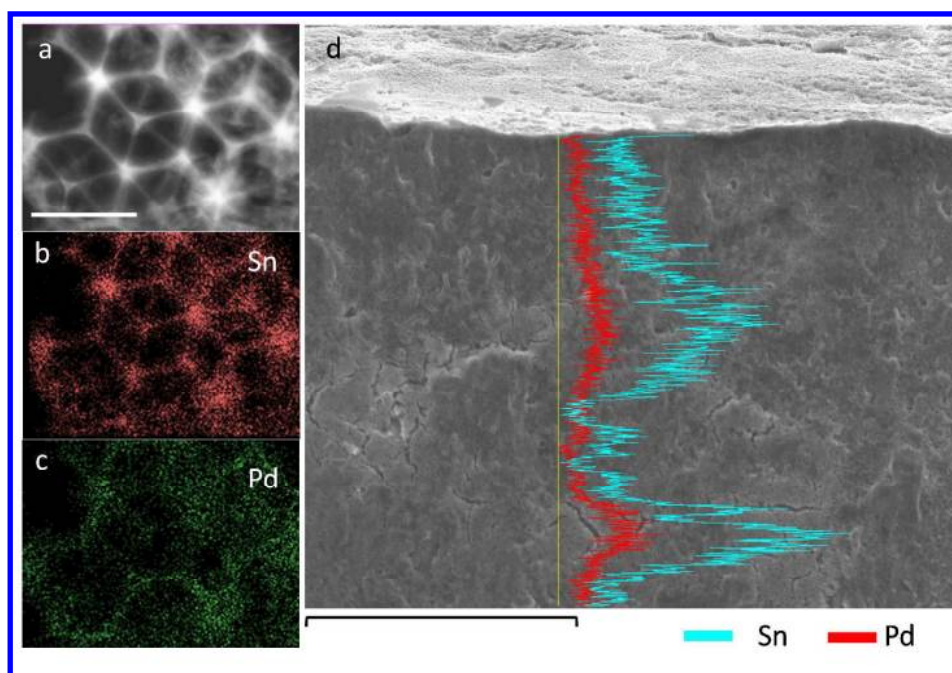


Figure 5. (a) STEM image of Pd deposited on SnO₂ IO at its (111) orientation. Scale bar = 500 nm. Corresponding elemental maps are shown for (b) Sn and (c) Pd. (d) Cross sectional SEM image of SnO₂-Pd IOs and EDX overlaying line scans for Sn and Pd. Scale bar in (d) is 100 μ m.

Achieving good dispersion of colloidal nanoparticles on porous supports can be hindered by poor wetting, unfavourable ligand-support interactions and high surface tension solvents limiting penetration into porous supports. Gupta and co-workers⁴⁵ reported high loadings of colloidal FePt nanoparticles onto SiO₂ surfaces, which they attribute to the short range specific interactions between the metal and support, facilitated by the presence of weakly binding oleic acid and oleylamine ligands. This immobilization method relies on the repulsive interactions between the hydrophobic ligands and hydrophilic oxide being much weaker than those between the highly polarizable metal NP and oxide surface. To investigate the influence the capping ligand in the Pd-SnO₂ system, Pd NPs capped with polyvinylpyrrolidone (PVP) ligands in aqueous ethanol solutions were immobilized into

SnO₂ IOs using the same procedure as OA-Pd NPs (Supporting Information Figure S9). EDX analysis showed negligible coverage by Pd of the SnO₂ IO supports. While OA is a weakly binding ligand readily exchanged by organic and inorganic ligands^{46, 47}, PVP is a significantly bulkier capping ligand which screens the interaction between the NP and the surface, consequently, the NPs do not immobilize on the surface or are more easily removed during rinsing. Stucky *et al.*⁴⁸ demonstrated that a homogenous dispersion of hydrophobic dodecanethiol capped Au NPs in aprotic solvents can be achieved on oxide supports by this approach. While their procedure allowed for homogenous dispersion, calcination was still required to 'lock in' the dispersed NPs. Post-annealing treatments, which are typically > 300 °C, are not required for the immobilization of Pd NPs onto the SnO₂ IO, which were subject to heating at much lower temperature of 120 °C. The inherent roughness of the nanostructured SnO₂ surface, porosity and the comparable size of the Pd NPs and SnO₂ crystallites, as well as weak ligand interactions all contribute to the uniform dispersion and adhesion of the Pd NPs.

To further understand the immobilization of Pd on SnO₂ IOs, the nature of the Pd – SnO₂ interaction was probed by XPS analysis. Chemical compositional analysis of the as-synthesized and SnO₂ immobilized Pd NPs was determined by XPS, shown in figure 6. The Pd 3d core level spectrum of OA-Pd NPs show a doublet at a binding energy of 335.1 eV and 340.4 eV, which can be assigned to metallic Pd 3d_{5/2} and 3d_{3/2}, respectively. There is also the presence of a shoulder peak at a binding energy of 336.3 eV which can be assigned to PdO⁴⁹. Analysis of Pd 3d spectra for Pd NPs deposited on SnO₂ IOs also show the presence of Pd(0) and Pd(II) species, with an additional peak at a binding energy of 338 eV, associated with highly oxidized Pd⁴⁺ species such as PdO₂^{50, 51}, however, the presence of Pd⁴⁺ hydroxide species have also been reported in the range of 337.9-338.5 eV⁵². PdO₂ is unstable in its anhydrous form but has been observed on Pd NPs stabilized by a surrounding oxide matrix.

^{51, 53, 54} Formation of PdO₂ may occur due to reaction with hydroxyl groups on the SnO₂ surface. Immobilization of the Pd NPs onto SnO₂ IOs gave rise to peak broadening, which has been associated with surface oxidation.⁵⁵ The fraction of Pd⁰ and Pd²⁺ species of the as-synthesized OA-Pd NPs determined from the integrated Pd 3d peak intensities, are 0.74 and 0.26, respectively. After NP immobilization, the fraction of Pd species is 0.73 (Pd⁰), 0.16 (Pd²⁺) and 0.11 (Pd⁴⁺) suggesting that the formation of Pd⁴⁺ is mainly at the expense of Pd²⁺ oxide species. Calculation of the oxide thickness from the combined Pd²⁺ and Pd⁴⁺ intensities, using Eqns 1 and 2, yields an effective oxide thickness of 0.91 nm averaged for all NPs. The curvature of nanoparticles however leads to an overestimate in the oxide thickness determined by XPS intensities and a geometric correction is required to account for the enhanced sensitivity of the oxide overlayer.⁵⁶ Using the correction factor for Pd nanoparticles derived by Van Devener *et al.*⁵⁷ the estimated oxide thickness of Pd NPs on SnO₂ IOs is 0.38 nm, essentially one monolayer of oxide.

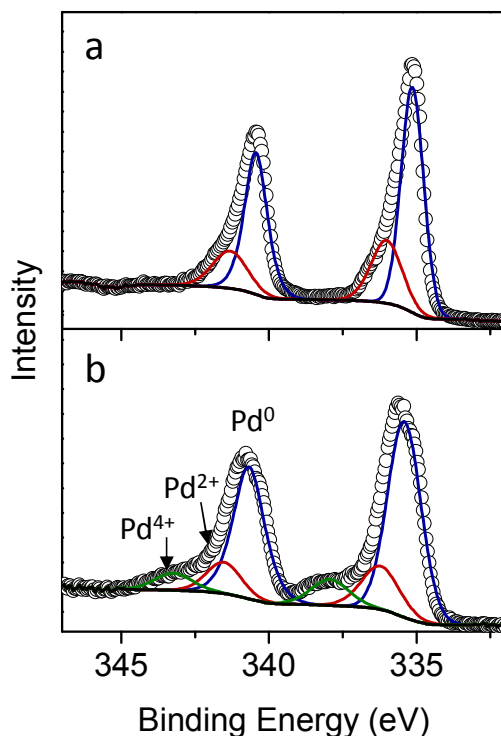


Figure 6. Pd 3d core-level spectra of (a) as-prepared OA-Pd NPs and (b) after immobilization onto SnO₂ IOs.

Analysis of the Sn 3d core level spectrum after Pd NP immobilization (Supporting Information Figure S10) displays a binding energy shift of +0.4 eV. This peak shift may be attributed to an interaction between Pd and SnO₂, manifest in shifts in core level binding energy.^{58, 59} The observed peak shifts may also correspond to changes in the Snⁿ⁺ oxidation state.^{60, 61} The electronic interaction between the SnO₂ and Pd NPs as well formation of oxide as detected by XPS may also contribute to anchoring Pd NPs to the surface.

In addition to changes in the Pd surface chemistry, immobilization of the NPs was also found to alter the chemistry of the oleylamine capping ligands. Figure 7 compares the N 1s core-level spectra of the as prepared OA-Pd NPs and is characterized by a single peak located at a binding energy of 399.8 eV. This energy is characteristic of alkylamine adsorption on Pd and is consistent with the FTIR analysis indicating that OA ligands absorb with the –NH₂ group intact.⁶² After immobilization onto SnO₂ IOs, the N 1s spectrum shows the amine-associated peak at 399.8 eV and a second, lower intensity peak at a binding energy of 398.2 eV, which is associated with unsaturated N species.⁶³ The presence of imine (–N=C), nitriles (N≡C) and keteneimine (C=C=N) groups have been reported due to irradiation damage during XPS collection⁶³. If this peak (398.2 eV) was induced by X-ray irradiation, its presence would also be expected in the pure OA-Pd NPs, which is not the case. Formation of nitriles and imines from aliphatic amines has been reported in the synthesis of Ag and Fe NPs.^{40, 64} The weak binding strength of OA may result in migration of the amine from the NP surface to the surrounding support leading to reactions with the oxide surface.

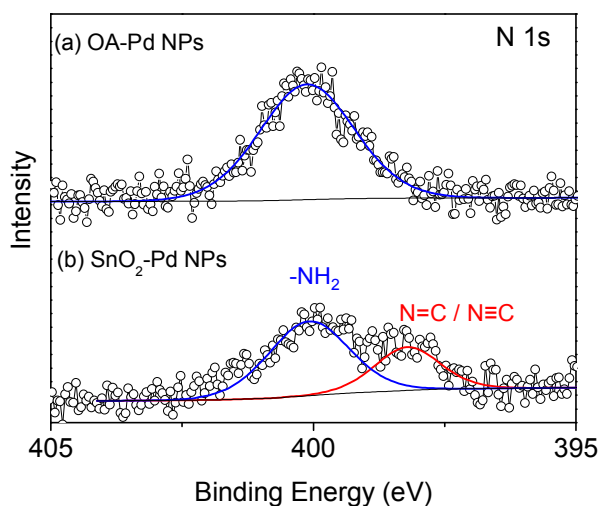


Figure 7. N 1s core level spectra of (a) OA-Pd NPs and (b) Pd-SnO₂ IOs.

A further benefit of using a weakly binding capping ligand such as OA is the potential to remove the ligand by treatment with acetic acid.³¹ XPS analysis of the SnO₂-Pd IOs refluxed in acetic acid for 12 h show a 42% decrease in the Pd:N ratio indicating considerable loss of the capping ligands (Supporting Information, Figure S11). It is however worth noting that the use of OA as a capping ligand do not significantly impact on the catalytic performance.⁴¹

Catalytic Performance of SnO₂-Pd IOs

Heterogeneous catalysts with hierarchical structures are particularly beneficial for liquid phase reactions where mass transfer limitations can be problematic with the use of micro/nanoporous supports. The performance of SnO₂-Pd IOs as catalytic coatings were evaluated in Suzuki coupling reactions as shown in Table 1. The SnO₂-Pd IOs show excellent reactivity in cross coupling of aryl iodides and bromides with phenylboronic acid

obtaining yields > 90% under air and at room temperature. Furthermore, the catalyst does not require any separation procedure after the reaction expect form removal of the stainless steel substrate. The reusability of the catalyst was also evaluated in cross coupling of 4-methoxyiodobenzene and phenylboronic acid at room temperature. The catalyst showed excellent recyclability over 3 cycles showing no loss in catalytic activity with yields of 95% \pm 3% (determined by GC using internal standard). Ellis *et al.*⁶⁵ found high reactivity associated with the edge and corner atoms of NPs in heterogeneously catalysed Suzuki coupling reactions, thus the presence of small diameter NPs as are immobilized on the IOs contain a higher proportion of these defect sites compared to larger diameter NPs. Furthermore, increased accessibility of these active sites may be facilitated by the hierarchical porous SnO₂ network. A major drawback of the use of unsupported colloidal NPs is that their solubility is influence by the nature of the capping ligands, therefore the unsupported NPs readily aggregate when added to the aqueous reaction due to the hydrophobic OA ligands (Supporting Information, Figure S12). To investigate the effect of the porosity, a non-porous SnO₂ film was prepared and subjected to the same Pd NP deposition. SEM of the SnO₂ (Supporting Information Figure S13) shows no obvious porosity in the film and EDX analysis (Figure S14) after Pd deposition reveals the presence of NPs on the surface of the film. The non-porous SnO₂ film gave a reasonably good yield (84%, determined by GC), although lower compared to the SnO₂ IOs, on the first cycle. The non-porous SnO₂ films showed poor recyclability and decreased catalytic performance after the first cycle, with the yield dropping to 43% in the second cycle. Suzuki coupling conditions have been reported to give rise to Pd leaching, thus the poor reusability is likely to be associated with loss of the active metal.⁶⁶ Furthermore, immobilization of NPs onto oxide support materials have been shown to increase instability of and leaching resistance of the catalyst.⁶⁷

Table 1. Suzuki cross coupling reactions catalyzed by SnO₂ Pd IOs.

Aryl Halide	Time (h)	Temperature °C	Yield % ^[a]	TON	TOF ^{tot} (h ⁻¹) ^[b]
	3 h	20	93	11923	3974
	4 h	20	92	11795	2949
	1 h	80	95	12179	12179
	4 h	20	85	10897	2724

Conditions: aryl halide (2 mmol), phenylboronic acid (2.2 mmol), K₂CO₃ (2 equivalents), EtOH:H₂O (2:1). ^[a] Isolated yield. ^[b] The TOF calculated from the total mass of Pd estimated from the mass of SnO₂ IO thin film, assuming 10 wt% Pd.

The electrocatalytic activity of the SnO₂-Pd IOs was also investigated for formic acid oxidation (FAO). Figure 8 shows the linear sweep voltammograms (LSVs) for SnO₂ Pd IOs and commercially available Pd/C in 2 M HCOOH + 0.1 M HClO₄. The SnO₂ Pd IOs display a well-defined anodic peak at 0.09 V, attributed to oxidation of formic acid catalyzed by the Pd NPs.²⁸ Furthermore, the onset potential of formic acid oxidation is ~ 180 mV lower in SnO₂ Pd IOs compared to commercial Pd/C which occurs at 0.2 V. The inset in figure 8 shows CVs for SnO₂ IOs in the absence of Pd NPs; it is clear that no oxidation of formic acid occurs and that SnO₂ support does not results in side reactions in the anodic response of the

polarization curve. It is well recognized that FAO is dependent on the nanoparticle size for a given density and dispersion.⁶⁸ TEM analysis of the commercial Pd/C shows Pd NPs with a diameter of 2-5 nm, however the presence of larger Pd aggregates in this composite is also evident (Supporting Information Figure S15). Better diameter control of the Pd NPs (consistency in shape, size and dispersion) supported on SnO₂ IOs facilitated by the assembly around the walls of the hierarchical morphology of the SnO₂ IO results in a greater proportion of electrochemically active Pd sites, while electrical contact required for electrochemical activity is maintained by their immobilization on to the interconnected SnO₂ nanocrystals.

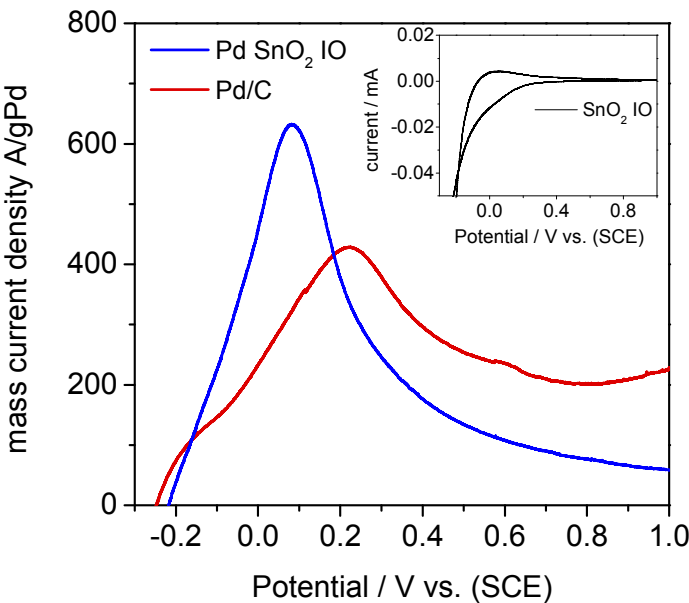


Figure 8. Linear sweep voltammogram of formic acid oxidation using Pd SnO₂ IOs. The inset shows the CV curve for blank SnO₂ IO before Pd NP immobilization.

Conclusions

We have demonstrated that a high surface area of interconnected phase-pure SnO₂ nanocrystals, formed as a continuous inverted opal network, is possible using tin acetate. The

structure exhibits hierarchical porosity on multiple lengths scales (cm down to nm). The thickness of the IO wall structure comprising nanocrystals of the oxide can be tuned by multiple infilling of the precursor. Uniform dispersion of highly uniform and dispersed assemblies of Pd NPs on the SnO₂ IO support is achieved by exploiting the relatively weak binding affinity between the OA capping ligand and the Pd NPs dispersed in a low surface tension solvent. The result is an ordered Pd NP assembly around the walls of the IO structure, accessible to liquids and gases. The catalytic performance of the SnO₂-Pd IOs was assessed in Suzuki cross coupling reactions and found to display excellent activity at room temperature with no loss of catalytic activity after 3 cycles. The SnO₂-Pd IOs also show potential for fuel cell applications and in electrocatalytic oxidation reactions, with improved formic acid oxidation demonstrated with the SnO₂-Pd IOs. The enhanced catalytic performance is attributed to the uniform dispersion of small diameter Pd NPs and the hierarchical porosity throughout the IO network, facilitating access to the catalytically active sites. The programmable porous order and the porosity possible at multiple length scale augers well for a range of catalytic process involving liquids and gases, and scope exists for the immobilization of a wide range of high index facet catalytic materials is programmable, ordered porous host structures. The high density of available catalytic sites in an order porous network has not been previously demonstrated for supported catalysts, which represent the primary catalyst in industrial oxidation and catalytic reactions.

Acknowledgments

We acknowledge financial support from Science Foundation Ireland under award nos 07/SK/B1232a and 08/CE/I1432. This research was also enabled by the UCC Strategic Research Fund, the Irish Research Council (IRC) New Foundations Award 2012 and the

Higher Education Authority Program for Research in Third Level Institutions (2007-2011) via the INSPIRE programme. MO acknowledges the support of IRC under award no. RS/2010/2170. The authors also thank Dr Fathima Laffir for her assistance with XPS measurements.

Supporting Information

This information is available free of charge via the Internet at <http://pubs.acs.org/>.

References

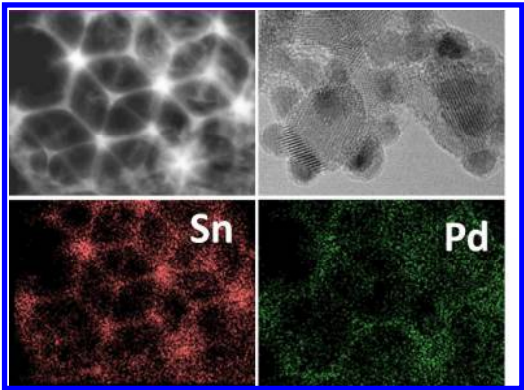
1. Hatton, B.; Mishchenko, L.; Davis, S.; Sandhage, K. H.; Aizenberg, J., Assembly of large-area, highly ordered, crack-free inverse opal films. *Proc. Nat. Acad. Sci. USA* **2010**, 107, (23), 10354-10359.
2. Huang, J. Y.; Zhong, L.; Wang, C. M.; Sullivan, J. P.; Xu, W.; Zhang, L. Q.; Mao, S. X.; Hudak, N. S.; Liu, X. H.; Subramanian, A.; Fan, H.; Qi, L.; Kushima, A.; Li, J., In Situ Observation of the Electrochemical Lithiation of a Single SnO₂ Nanowire Electrode. *Science* **2010**, 330, (6010), 1515-1520.
3. Han, S. J.; Jang, B. C.; Kim, T.; Oh, S. M.; Hyeon, T., Simple synthesis of hollow tin dioxide microspheres and their application to lithium-ion battery anodes. *Adv. Funct. Mater.* **2005**, 15, (11), 1845-1850.
4. Liu, R.; Yang, S. C.; Wang, F.; Lu, X. G.; Yang, Z. M.; Ding, B. J., Sodium Chloride Template Synthesis of Cubic Tin Dioxide Hollow Particles for Lithium Ion Battery Applications. *ACS Appl. Mater. Interfaces* **2012**, 4, (3), 1537-1542.
5. Yu, J.; Zhao, D.; Xu, X.; Wang, X.; Zhang, N., Study on RuO₂/SnO₂: Novel and Active Catalysts for CO and CH₄ Oxidation. *Chemcatchem* **2012**, 4, (8), 1122-1132.
6. Aruna, I.; Kruis, F. E.; Kundu, S.; Muhler, M.; Theissmann, R.; Spasova, M., CO ppb sensors based on monodispersed SnO(x):Pd mixed nanoparticle layers: Insight into dual conductance response. *J. Appl. Phys.* **2009**, 105, (6).
7. Epifani, M.; Arbiol, J.; Pellicer, E.; Comini, E.; Siciliano, P.; Faglia, G.; Morante, J. R., Synthesis and gas-sensing properties of pd-doped SnO₂ nanocrystals. A case study of a general methodology for doping metal oxide nanocrystals. *Cryst. Growth Des.* **2008**, 8, (5), 1774-1778.
8. Lee, H.; Kang, C.-M.; Park, M.; Kwak, J.; Lee, C., Improved efficiency of inverted organic light-emitting diodes using tin dioxide nanoparticles as an electron injection layer. *ACS Appl. Mater. Interfaces* **2013**, 5, (6), 1977-81.
9. Wang, Y.-F.; Li, J.-W.; Hou, Y.-F.; Yu, X.-Y.; Su, C.-Y.; Kuang, D.-B., Hierarchical Tin Oxide Octahedra for Highly Efficient Dye-Sensitized Solar Cells. *Chem. Eur. J.* **2010**, 16, (29), 8620-8625.
10. Martinez, C. J.; Hockey, B.; Montgomery, C. B.; Semancik, S., Porous tin oxide nanostructured microspheres for sensor applications. *Langmuir* **2005**, 21, (17), 7937-7944.
11. D'Arienzo, M.; Armelao, L.; Cacciamani, A.; Mari, C. M.; Polizzi, S.; Ruffo, R.; Scotti, R.; Testino, A.; Wahba, L.; Morazzoni, F., One-Step Preparation of SnO₂ and Pt-Doped SnO₂ As Inverse Opal Thin Films for Gas Sensing. *Chem. Mater.* **2010**, 22, (13), 4083-4089.
12. Scott, R. W. J.; Yang, S. M.; Chabanis, G.; Coombs, N.; Williams, D. E.; Ozin, G. A., Tin dioxide opals and inverted opals: Near-ideal microstructures for gas sensors. *Adv. Mater.* **2001**, 13, (19), 1468-+.

13. Parlett, C. M. A.; Wilson, K.; Lee, A. F., Hierarchical porous materials: catalytic applications. *Chem. Soc. Rev.* **2013**, 42, 3876-3893.
14. Klaewkla, R.; Arend, M.; Hoelderich, W. F., *A Review of Mass Transfer Controlling the Reaction Rate in Heterogeneous Catalytic Systems*. InTech: 2011.
15. Pirez, C.; Caderon, J.-M.; Dacquin, J.-P.; Lee, A. F.; Wilson, K., Tunable KIT-6 Mesoporous Sulfonic Acid Catalysts for Fatty Acid Esterification. *ACS Catalysis* **2012**, 2, (8), 1607-1614.
16. Parlett, C. M. A.; Bruce, D. W.; Hondow, N. S.; Lee, A. F.; Wilson, K., Support-Enhanced Selective Aerobic Alcohol Oxidation over Pd/Mesoporous Silicas. *ACS Catalysis* **2011**, 1, (6), 636-640.
17. Chen, Y.-X.; Lavacchi, A.; Chen, S.-P.; di Benedetto, F.; Bevilacqua, M.; Bianchini, C.; Fornasiero, P.; Innocenti, M.; Marelli, M.; Oberhauser, W.; Sun, S.-G.; Vizza, F., Electrochemical Milling and Faceting: Size Reduction and Catalytic Activation of Palladium Nanoparticles. *Angew. Chem.-Int. Edit.* **2012**, 51, (34), 8500-8504.
18. Diaz, C.; Valenzuela, M. L.; Bravo, D.; Dickinson, C.; O'Dwyer, C., Solid-state synthesis of embedded single-crystal metal oxide and phosphate nanoparticles and in situ crystallization. *J. Colloid Interface Sci.* **2011**, 362, (1), 21-32.
19. Murray, C. B.; Kagan, C. R.; Bawendi, M. G., Synthesis and characterization of monodisperse nanocrystals and close-packed nanocrystal assemblies. *Annu. Rev. Mater. Sci.* **2000**, 30, 545-610.
20. Antolini, E., Carbon supports for low-temperature fuel cell catalysts. *Appl. Catal., B* **2009**, 88, (1-2), 1-24.
21. Mukhopadhyay, K.; Phadtare, S.; Vinod, V. P.; Kumar, A.; Rao, M.; Chaudhari, R. V.; Sastry, M., Gold nanoparticles assembled on amine-functionalized Na-Y zeolite: A biocompatible surface for enzyme immobilization. *Langmuir* **2003**, 19, (9), 3858-3863.
22. Sayo, K.; Deki, S.; Hayashi, S., Supported gold catalysts prepared by using nano-sized gold particles dispersed in nylon-11 oligomer. *J. Mater. Chem.* **1999**, 9, (4), 937-942.
23. Menard, L. D.; Xu, F.; Nuzzo, R. G.; Yang, J. C., Preparation of TiO₂-supported Au nanoparticle catalysts from a Au-13 cluster precursor: Ligand removal using ozone exposure versus a rapid thermal treatment. *J. Catal.* **2006**, 243, (1), 64-73.
24. Aliaga, C.; Park, J. Y.; Yamada, Y.; Lee, H. S.; Tsung, C.-K.; Yang, P.; Somorjai, G. A., Sum Frequency Generation and Catalytic Reaction Studies of the Removal of Organic Capping Agents from Pt Nanoparticles by UV-Ozone Treatment. *J. Phys. Chem. C* **2009**, 113, (15), 6150-6155.
25. Lopez-Sanchez, J. A.; Dimitratos, N.; Hammond, C.; Brett, G. L.; Kesavan, L.; White, S.; Miedziak, P.; Tiruvalam, R.; Jenkins, R. L.; Carley, A. F.; Knight, D.; Kiely, C. J.; Hutchings, G. J., Facile removal of stabilizer-ligands from supported gold nanoparticles. *Nat. Chem.* **2011**, 3, (7), 551-556.
26. Zhang, P.; Huang, S.-Y.; Popov, B. N., Mesoporous Tin Oxide as an Oxidation-Resistant Catalyst Support for Proton Exchange Membrane Fuel Cells. *J. Electrochem. Soc.* **2010**, 157, (8), B1163-B1172.
27. Ortel, E.; Sokolov, S.; Zielke, C.; Lauermann, I.; Selve, S.; Weh, K.; Paul, B.; Polte, J.; Kraehnert, R., Supported Mesoporous and Hierarchical Porous Pd/TiO₂ Catalytic Coatings with Controlled Particle Size and Pore Structure. *Chemistry of Materials* **2012**, 24, (20), 3828-3838.
28. Lu, H.; Fan, Y.; Huang, P.; Xu, D., SnO₂ nanospheres supported Pd catalyst with enhanced performance for formic acid oxidation. *Journal of Power Sources* **2012**, 215, 48-52.
29. Kumar, A.; Pandey, A. C.; Prakash, R., Electro-oxidation of formic acid using polyindole-SnO₂ nanocomposite. *Catalysis Science & Technology* **2012**, 2, (12), 2533-2538.
30. Rogach, A. L.; Kotov, N. A.; Koktysh, D. S.; Ostrander, J. W.; Ragoisha, G. A., Electrophoretic deposition of latex-based 3D colloidal photonic crystals: A technique for rapid production of high-quality opals. *Chem. Mater.* **2000**, 12, (9), 2721-2726.
31. Mazumder, V.; Sun, S., Oleylamine-Mediated Synthesis of Pd Nanoparticles for Catalytic Formic Acid Oxidation. *J. Am. Chem. Soc.* **2009**, 131, (13), 4588-+.
32. Yang, Z.; Klabunde, K. J., Synthesis of nearly monodisperse palladium (Pd) nanoparticles by using oleylamine and trioctylphosphine mixed ligands. *J. Organomet. Chem.* **2009**, 694, (7-8), 1016-1021.

33. Teranishi, T.; Miyake, M., Size control of palladium nanoparticles and their crystal structures. *Chem. Mater.* **1998**, 10, (2), 594-600.
34. Briggs, D.; Seah, M. P., *Practical Surface Analysis by Auger and X-ray Photoelectron Spectroscopy*. John Wiley and Sons: 1983.
35. Shaplygin, I. S.; Aparnikov, G. L.; Lazarev, V. B., Preparation of palladium dioxide at high pressure. *Zh. Neorg. Khim.* **1978**, 23, (4), 884-887.
36. Cumpson, P. J.; Seah, M. P., Elastic scattering corrections in AES and XPS .2. Estimating attenuation lengths and conditions required for their valid use in overlayer/substrate experiments. *Surf. Interface Anal.* **1997**, 25, (6), 430-446.
37. Mazumder, V.; Chi, M.; Mankin, M. N.; Liu, Y.; Metin, O.; Sun, D.; More, K. L.; Sun, S., A Facile Synthesis of MPd (M = Co, Cu) Nanoparticles and Their Catalysis for Formic Acid Oxidation. *Nano Letters* **2012**, 12, (2), 1102-1106.
38. Dai, Z. R.; Gole, J. L.; Stout, J. D.; Wang, Z. L., Tin oxide nanowires, nanoribbons, and nanotubes. *J. Phys. Chem. B* **2002**, 106, (6), 1274-1279.
39. Batzill, M.; Diebold, U., The surface and materials science of tin oxide. *Prog. Surf. Sci.* **2005**, 79, (2-4), 47-154.
40. Chen, M.; Feng, Y.-G.; Wang, X.; Li, T.-C.; Zhang, J.-Y.; Qian, D.-J., Silver nanoparticles capped by oleylamine: Formation, growth, and self-organization. *Langmuir* **2007**, 23, (10), 5296-5304.
41. Mourdikoudis, S.; Liz-Marzán, L. M., Oleylamine in Nanoparticle Synthesis. *Chem. Mater.* **2013**, 25, (9), 1465-1476.
42. Ho, S. Y.; Wong, A. S. W.; Ho, G. W., Controllable Porosity of Monodispersed Tin Oxide Nanospheres via an Additive-Free Chemical Route. *Cryst. Growth Des.* **2009**, 9, (2), 732-736.
43. Cai, Z.; Teng, J.; Xiong, Z.; Li, Y.; Li, Q.; Lu, Z.; Zhao, X. S., Fabrication of TiO₂ Binary Inverse Opals without Overlayers via the Sandwich-Vacuum Infiltration of Precursor. *Langmuir* **2011**, 27, 5157-5164.
44. Meynen, V.; Cool, P.; Vansant, E. F., Verified syntheses of mesoporous materials. *Microporous Mesoporous Mater.* **2009**, 125, (3), 170-223.
45. Gupta, G.; Patel, M. N.; Ferrer, D.; Heitsch, A. T.; Korgel, B. A.; Jose-Yacaman, M.; Johnston, K. P., Stable ordered FePt mesoporous silica catalysts with high loadings. *Chem. Mater.* **2008**, 20, (15), 5005-5015.
46. Dong, A.; Ye, X.; Chen, J.; Kang, Y.; Gordon, T.; Kikkawa, J. M.; Murray, C. B., A Generalized Ligand-Exchange Strategy Enabling Sequential Surface Functionalization of Colloidal Nanocrystals. *J. Am. Chem. Soc.* **2011**, 133, (4), 998-1006.
47. Niu, Z.; Peng, Q.; Gong, M.; Rong, H.; Li, Y., Oleylamine-Mediated Shape Evolution of Palladium Nanocrystals. *Angew. Chem.-Int. Edit.* **2011**, 50, (28), 6315-6319.
48. Zheng, N.; Stucky, G. D., A general synthetic strategy for oxide-supported metal nanoparticle catalysts. *J. Am. Chem. Soc.* **2006**, 128, (44), 14278-14280.
49. Pillo, T.; Zimmermann, R.; Steiner, P.; Hufner, S., The electronic structure of PdO found by photoemission (UPS and XPS) and inverse photoemission (BIS). *Journal of Physics-Condensed Matter* **1997**, 9, (19), 3987-3999.
50. Kibis, L. S.; Stadnichenko, A. I.; Koscheev, S. V.; Zaikoyskii, V. I.; Boronin, A. I., Highly Oxidized Palladium Nanoparticles Comprising Pd⁴⁺ Species: Spectroscopic and Structural Aspects, Thermal Stability, and Reactivity. *J. Phys. Chem. C* **2012**, 116, (36), 19342-19348.
51. Kibis, L. S.; Titkov, A. I.; Stadnichenko, A. I.; Koscheev, S. V.; Boronin, A. I., X-ray photoelectron spectroscopy study of Pd oxidation by RF discharge in oxygen. *Appl. Surf. Sci.* **2009**, 255, (22), 9248-9254.
52. Kim, K. S.; Gossmann, A. F.; Winograd, N., X-ray photoelectron spectroscopic studie of palladium oxides and palladium oxygen electrode. *Anal. Chem.* **1974**, 46, (2), 197-200.
53. Otto, K.; Haack, L. P.; Devries, J. E., Identification of 2 types of oxidied Pd on gamma alumina by XPS. *Appl. Catal. B* **1992**, 1, (1), 1-12.

54. Sohn, Y.; Pradhan, D.; Leung, K. T., Electrochemical Pd Nanodeposits on a Au Nanoisland Template Supported on Si(100): Formation of Pd-Au Alloy and Interfacial Electronic Structures. *ACS Nano* **2010**, 4, (9), 5111-5120.
55. Wang, J.; Yun, Y.; Altman, E. I., The plasma oxidation of Pd(100). *Surf. Sci.* **2007**, 601, (16), 3497-3505.
56. Mohai, M.; Bertoti, I., Calculation of overlayer thickness on curved surfaces based on XPS intensities. *Surf. Interface Anal.* **2004**, 36, (8), 805-808.
57. Van Devener, B.; Anderson, S. L.; Shimizu, T.; Wang, H.; Nabity, J.; Engel, J.; Yu, J.; Wickham, D.; Williams, S., In Situ Generation of Pd/PdO Nanoparticle Methane Combustion Catalyst: Correlation of Particle Surface Chemistry with Ignition. *J. Phys. Chem. C* **2009**, 113, (48), 20632-20639.
58. Frolov, D. D.; Kotovshchikov, Y. N.; Morozov, I. V.; Boltalin, A. I.; Fedorova, A. A.; Marikutsa, A. V.; Rumyantseva, M. N.; Gaskov, A. M.; Sadovskaya, E. M.; Abakumov, A. M., Oxygen exchange on nanocrystalline tin dioxide modified by palladium. *J. Solid State Chem.* **2012**, 186, 1-8.
59. Schwartz, W. R.; Pfefferle, L. D., Combustion of Methane over Palladium-Based Catalysts: Support Interactions. *J. Phys. Chem. C* **2012**, 116, (15), 8571-8578.
60. He, M.; Yuan, L.; Hu, X.; Zhang, W.; Shu, J.; Huang, Y., A SnO₂@carbon nanocluster anode material with superior cyclability and rate capability for lithium-ion batteries. *Nanoscale* **2013**, 5, (8), 3298-3305.
61. Shanmugasundaram, A.; Basak, P.; Satyanarayana, L.; Manorama, S. V., Hierarchical SnO/SnO₂ nanocomposites: Formation of in situ p-n junctions and enhanced H₂ sensing. *Sensors and Actuators B-Chemical* **2013**, 185, 265-273.
62. Kumar, A.; Mandal, S.; Selvakannan, P. R.; Pasricha, R.; Mandale, A. B.; Sastry, M., Investigation into the interaction between surface-bound alkylamines and gold nanoparticles. *Langmuir* **2003**, 19, (15), 6277-6282.
63. Graf, N.; Yegen, E.; Gross, T.; Lippitz, A.; Weigel, W.; Krakert, S.; Terfort, A.; Unger, W. E. S., XPS and NEXAFS studies of aliphatic and aromatic amine species on functionalized surfaces. *Surf. Sci.* **2009**, 603, (18), 2849-2860.
64. Meffre, A.; Lachaize, S.; Gatel, C.; Respaud, M.; Chaudret, B., Use of long chain amine as a reducing agent for the synthesis of high quality monodisperse iron(0) nanoparticles. *J. Mater. Chem.* **2011**, 21, (35), 13464-13469.
65. Ellis, P. J.; Fairlamb, I. J. S.; Hackett, S. F. J.; Wilson, K.; Lee, A. F., Evidence for the Surface-Catalyzed Suzuki-Miyaura Reaction over Palladium Nanoparticles: An Operando XAS Study. *Angew. Chem. Int. Ed.* **2010**, 49, (10), 1820-1824.
66. Fang, P.-P.; Jutand, A.; Tian, Z.-Q.; Amatore, C., Au-Pd Core-Shell Nanoparticles Catalyze Suzuki-Miyaura Reactions in Water through Pd Leaching. *Angew. Chem.-Int. Edit.* **2011**, 50, (51), 12184-12188.
67. Zhang, N.; Xu, Y.-J., Aggregation- and Leaching-Resistant, Reusable, and Multifunctional Pd@CeO₂ as a Robust Nanocatalyst Achieved by a Hollow Core-Shell Strategy. *Chem. Mater.* **2013**, 25, (9), 1979-1988.
68. Zhou, W.; Lee, J. Y., Particle size effects in Pd-catalyzed electrooxidation of formic acid. *J. Phys. Chem. C* **2008**, 112, (10), 3789-3793.

TOC



1
2
3
4
5
6
7
8
9
10
11
12
13
14
15
16
17
18
19
20
21
22
23
24
25
26
27
28
29
30
31
32
33
34
35
36
37
38
39
40
41
42
43
44
45
46
47
48
49
50
51
52
53
54
55
56
57
58
59
60